ChemComm

Check for updates

Ambient electrosynthesis of urea with nitrate and carbon dioxide over a CuRu alloy catalyst†

Jiafang Liu, [ab] Shengbo Zhang, *[ab] Yong Jiang,[c] Wenyi Li,[ab] Meng Jin,[ab] Jun Ding,[ab] Yunxia Zhang, [ab] Guozhong Wang [ab] and Haimin Zhang *[ab]

Urea synthesis under mild conditions starting from the electrocatalytic coupling of carbon dioxide (CO_2) and nitrate represents a promising alternative experimentally to conquer the huge energy consumption in the industrial Haber–Bosch process. Herein, an electrocatalyst consisting of CuRu alloy nanoparticles on carbonized cellulose (CuRu-CBC) is designed and realizes the urea yield rate of 394.85 ± 16.19 µg h^{-1} mg$_{cat}$$^{-1}$ and an ultrahigh faradaic efficiency (FE) of $68.94 \pm 3.05\%$ at -0.55 V (vs. RHE) under ambient conditions. Further XAS analyses indicated that the favored internal electron transfer between Cu and Ru dual active sites significantly improved the C–N coupling activity. Various characterizations, including in situ ATR-SEIRAS and DEMS analysis highlighted the favorable generation of key intermediates *CO and *NH, making CuRu-CBC a promising catalyst for urea synthesis.

Urea, as a prevalent nitrogen-based fertilizer, plays a crucial role in the current chemical raw material market.[1,2] However, industrial-scale urea generation is conducted under highly demanding conditions (N_2 + H_2 → NH_3, 150–350 bar, 350-550 °C; NH_3 + CO_2 → $CO(NH_2)_2$, 150-250 bar, 150-200 °C), which require harsh reaction conditions and further result in intense energy consumption.[3,4] Therefore, an alternative solution is needed to allow urea synthesis driven by distributed clean energy sources.[5,6] Compared with the harsh industrial synthesis process, the production of urea through the electrocatalytic coupling of CO_2 and N-containing species (*e.g.*, N_2, NO_2^-, NO_3^-) represents a more efficient and green strategy.[7–10] This approach not only alleviates the fuels with high

energy density, but also contributes to progress toward the carbon-neutral goal, thereby achieving environmental conservation and pollutant mitigation, and fostering advancements in the urea industry.

To date, researchers have developed numerous electrocatalysts for electrocatalytic urea synthesis.[11–15] For instance, Wang *et al.*[11] successfully achieved electrocatalytic CO_2 and N_2 coupling for urea generation using alloy state Pd$_1$Cu$_1$ TiO$_2$-400 under mild conditions. The urea formation rate reached 3.36 mmol g^{-1} h^{-1} at -0.4 V (*vs.* RHE), with a corresponding faradaic efficiency (FE) of 8.92%. The lower urea yield and Faraday efficiency were attributed to the high bond energy (941 kJ mol^{-1}) of N≡N and the poor water solubility of N_2, leading to increased energy barriers for the hydrogenation process of reactants, which is unfavorable for efficient C–N coupling.[16] In contrast, NO_3^- (or NO_2^-) in aqueous electrolytes has been reported as a promising substitutional nitrogen source in electrocatalytic C–N coupling to form urea.[6,8,16,17] For instance, Yu and co-workers[6] prepared an In(OH)$_3$ electrocatalyst with well-defined facets, favoring the direct C–N coupling reaction between *NO$_2$ and *CO$_2$ intermediates and leading to selective electrochemical urea production from CO_2 and NO_3^- with remarkable Faraday efficiency (FE) of 53.4% and a urea yield of 533.1 µg h^{-1} mg$_{cat}$$^{-1}$ at -0.6 V (*vs.* RHE).

However, it is worth noting that the above-mentioned electrocatalysts possess only one kind of active site, so they usually have low efficiency in selectively adsorbing and activating two or more reactants simultaneously to accomplish C–C/C–N coupling reaction, which is not conductive to improving the urea production efficiency. Dual-site or multisite catalysts can effectively enhance surface charge transfer and co-adsorption of multiple reactants.[18–20] Thus, Wang *et al.*[21] integrated Fe and Ni sites into an isolated diatomic Fe–Ni electrocatalyst, which enables the simultaneously triggering of numerous activated C- and N-species and increases the possibility of encountering and coupling of these intermediate species to generate crucial C–N bonds, achieving the so far highest urea yield of 242 µg h^{-1} cm^{-2} from CO_2 and NO_3^-. Unfortunately, this newly developed diatomic Fe–

^{a} *Key Laboratory of Materials Physics, Centre for Environmental and Energy Nanomaterials, Anhui Key Laboratory of Nanomaterials and Nanotechnology, CAS Center for Excellence in Nanoscience Institute of Solid State Physics, HFIPS, Chinese Academy of Sciences, Hefei 230031, P. R. China. E-mail: shbzhang@issp.ac.cn, zhanghm@issp.ac.cn*

^{b} *University of Science and Technology of China, P. R. China*

^{c} *Shanghai Synchrotron Radiation Facility, Shanghai Advanced Research Institute, Chinese Academy of Sciences, Shanghai 201800, P. R. China*

† Electronic supplementary information (ESI) available. See DOI: https://doi.org/10.1039/d4cc04024d

Ni electrocatalyst still suffers from low FE ($<20\%$) and high overpotentials.[21] Therefore, it is still urgent to develop new electrocatalysts with multiple active sites for efficient urea production.

Currently, Cu-based materials are widely employed in electrocatalytic CO_2RR and NO_3RR, such as Cu SACs,[22] Cu SAAs,[16] and Cu alloys (PdCu,[11] CuRh,[14] CuNi[23] and CuCo[24]), which exhibit excellent reactivity due to their unique d-band centers. For the sake of achieving the construction of a dual active site electrocatalyst that simultaneously catalyzes CO_2 and NO_3^- for the direct synthesis of urea, an electrocatalyst consisting of CuRu alloy nanoparticles on carbonized cellulose (CuRu-CBC) was successfully prepared in this study. The electrocatalytic performance of CuRu-CBC in CO_2 and NO_3^- co-reduction to generate urea was tested under mild conditions. The prepared CuRu-CBC alloy catalyst exhibited a urea yield of 394.85 ± 16.19 µg h^{-1} mg$_{cat}^{-1}$ and an ultrahigh FE of $68.94 \pm 3.05\%$ at -0.55 V (vs. RHE). Further X-ray absorption spectroscopy (XAS) analyses indicated that the favored internal electron transfer between Ru and Cu dual active sites significantly improved the electrocatalytic C–N coupling activity and selectivity. In addition, in situ attenuated total reflection surface-enhanced infrared adsorption spectroscopy (ATR-SEIRAS) combined with different electrochemical mass spectrometry (DEMS) analysis demonstrated that *CO and *NH are the key intermediates in the electrocatalytic C–N coupling reaction of the CuRu-CBC alloy. This work is expected to provide valuable insights for future developments in electrocatalytic urea generation.

In this work, we report the utilization of bacterial cellulose (BC) as an adsorption regulator and O-rich carbon substrate source to synthesize Cu-CBC, CuRu-CBC and Ru-CBC samples (see Experimental details Section, ESI†). Scanning electron microscopy (SEM) (Fig. 1a) shows that the as-synthesized CuRu-CBC sample still maintains the initial fiber-like morphology of the pristine BC.[25] Fig. 1b illustrates that the CuRu nanoalloy is homogeneously dispersed on the CBC surface, with a size ranging between 1-10 nm. Similarly, Cu-CBC and Ru-CBC exhibited similar structures (Fig. S1, ESI†). The magnified lattice fringes observed by the high-resolution transmission TEM (HR-TEM) image showed a d-spacing distance of 0.198 nm (Fig. 1c), corresponding to the (101) crystallographic surface of the hexagonal phase Ru. Notably, it is smaller than the (101) lattice spacing of 0.204 nm for Ru-CBC (Fig. S1d, ESI†). This difference may be attributed to the smaller atomic radius of Cu compared to Ru.[26]

The EDS elemental mapping pattern in Fig. 1d–h confirmed a uniform CuRu distribution of bimetallic nanocatalysts on the CBC support and showed the homogeneous morphology of the CuRu alloy. Inductively coupled plasma atomic emission spectroscopy (ICP-AES) was employed to determine the composition of the catalyst (Table S1, ESI†). The results show that the contents of Cu and Ru in CuRu-CBC are 2.5% and 1.7%, respectively. Further structural analyses of the as-synthesized Cu-CBC, CuRu-CBC and Ru-CBC samples were conducted by X-ray diffraction (XRD), as illustrated in Fig. S2 (ESI†). The XRD patterns of Cu-CBC reveal distinct diffraction peaks corresponding to the Cu monomer (JCPDS No. 04-0836) at $43.2°$, $50.5°$ and $74.2°$, denoted as its (111), (200) and (220) crystal planes, respectively. Moreover, the Ru-CBC sample exhibits three diffraction peaks at $38.5°$, $44.1°$ and $69.5°$, corresponding to the (100), (101) and (110) crystal planes (JCPDS No. 06-0663), respectively. The XRD analysis of CuRu-CBC detected peaks at $38.4°$, $43.1°$, $44.0°$ and $69.4°$, primarily corresponding to the Ru monomer. This observation suggests that the introduction of Cu atoms induces lattice distortion in Ru, aligning with the results of HR-TEM.

To investigate the surface chemical composition and valence state of the prepared samples, X-ray photoelectron spectroscopy (XPS) analysis was conducted. The full XPS spectra revealed the presence of C, O, Cu and Ru elements (Fig. S3a, ESI†). For CuRu-CBC (Fig. S3b, ESI†), the characteristic peaks of Cu$^{0,1+}$ 2p$_{2/3}$ and 2p$_{1/2}$ appear at 932.8 eV and 952.6 eV, respectively. In addition to the features of Cu$^{0,1+}$, two peaks corresponding to Cu^{2+} appear at 934.7 eV and 954.8 eV in the Cu 2p XPS spectrum. Additionally, the Ru 3p peaks in Fig. S3c (ESI†) showed two sets of peaks at 465.9 eV and 486.7 eV (Ru 3p$_{3/2}$ and Ru 3p$_{1/2}$), corresponding to Ru^{4+}, while another set at 462.4 eV and 484.1 eV indicated Ru^0. The Ru 3d$_{5/2}$ peak at 280.6 eV further confirmed Ru^0 (Fig. S3d, ESI†).[27] Moreover, a C=O bond peak at 288.4 eV was identified, attributed to surface CO_2 on CuRu-CBC. Notably, the Cu 2p electron binding energy was higher in the Cu-CBC sample (Cu 2p$_{3/2}$: 933.7 eV, Cu 2p$_{1/2}$: 953.6 eV) compared to CuRu-CBC. Conversely, the electronic binding energies of Ru 3p in the Ru-CBC samples (Ru 3p$_{3/2}$: 462.4 eV, 465.7 eV, Ru 3p$_{1/2}$: 483.9 eV, 486.4 eV) were slightly smaller than those in CuRu-CBC, suggesting interactions within the CuRu nanoalloy. Under an applied electric field, electrons were more favorable to accumulate on the surface of the Cu atoms. In the X-ray absorption near-edge spectra (XANES) of the Ru K-edge (Fig. 2a and inset) and the Cu K-edge (Fig. 2c and inset), a shift of the absorbing edge to the high-energy direction confirmed charge transfer. The Ru K-edge near-edge in CuRu-CBC resembled that of RuO_2, indicating a similar valence state. Similarly, the Cu K-edge near-edge in CuRu-CBC located between Cu foil and CuO, suggesting a valence state between 0 and +2. Fourier-transformed Ru K-edge extended X-ray absorption fine structure (EXAFS) spectra (Fig. 2b) indicated Ru coordination primarily with metallic Cu or Ru (Ru–M). Similar coordination was observed in Cu coordination for CuRu-CBC (Fig. 2d). Importantly, the interatomic distances $R_{Cu-M(Cu/Ru)}$ and $R_{Ru-M(Cu/Ru)}$ in CuRu-CBC were shorter than R_{Cu-Cu} in Cu foil and R_{Ru-Ru} in Ru foil, providing a structural basis for the CO_2 and NO_3^- co-reduction.[28] The N_2 adsorption–desorption isotherm measurement results (Fig. S5, ESI†) indicated that the BET
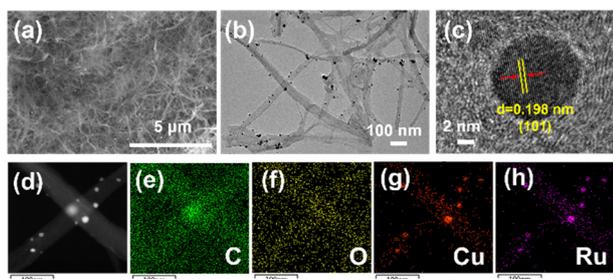

Fig. 1 (a) SEM, (b) TEM, (c) HRTEM and (d)–(h) EDS elemental mapping images of CuRu-CBC.
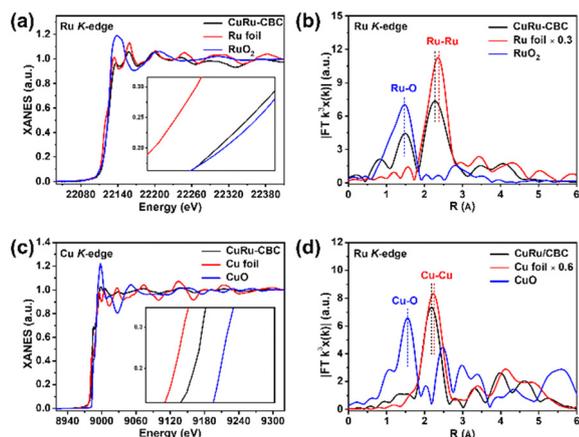
Fig. 2 (a) Ru K-edge XANES spectra of ordered CuRu-CBC (Ru foil and RuO$_2$ as reference), with a zoomed-in view of the Ru K-edge as the inset. (b) EXAFS Fourier-transformed k^3-weighted $\chi(k)$ function spectra of CuRu-CBC (Ru foil and RuO$_2$ as reference). (c) Cu K-edge XANES spectra of ordered CuRu-CBC (Cu foil and CuO as reference), with a zoomed-in view of the Ru K-edge as the inset. (d) EXAFS Fourier-transformed k^3-weighted $\chi(k)$ function spectra of CuRu-CBC (Cu foil and CuO as a reference).

surface area is 154.1, 93.0 and 94.1 m^2 g^{-1} for Cu-CBC, CuRu-CBC and Ru-CBC with microporous and mesoporous structures, which are beneficial to exposure of the active sites and the mass transport of electrolytes during electrolysis.

The prepared Cu-CBC, CuRu-CBC and Ru-CBC samples were subsequently evaluated for their activity in the electrocatalytic C–N coupling reaction for urea production. Electrochemical measurements were carried out in an H-type configuration with three electrodes. Linear scanning voltammetry (LSV) tests were performed to evaluate the electrochemical activity of CuRu-CBC (Fig. 3a). Notably, the current density over CuRu-CBC in Ar-saturated 0.1 M KNO$_3$ is higher than that in CO$_2$-saturated 0.1 M KNO$_3$, implying that CO$_2$ reduction (CO$_2$RR) or C–N coupling reactions may occur in the system while inhibiting other reactions, which is consistent with previous reports. To eliminate the influence of the C–N coupling by-product NO$_2^-$ on urea detection, the urea yield produced by electrocatalytic C–N coupling in Cu-CBC, CuRu-CBC and Ru-CBC samples was examined using the urease method (Fig. S6, ESI†). By-products NH$_4^+$ and NO$_2^-$ were detected using a colorimetric method, while CO and H$_2$ were detected by gas chromatography (Fig. S6–S8, ESI†). As shown in Fig. 3b, the performance of CuRu-CBC electrocatalytic urea synthesis was evaluated over a range of different applied potentials (repeated three times), and both the urea yield rate and FE show a volcanic curve and reach the maximum value of 394.85 ± 16.19 µg h^{-1} mg$_{cat}^{-1}$ and 68.94 ± 3.05% at the optimum applied potential of −0.55 V (*vs.* RHE). This is superior to most of the catalysts that have been reported for the electrochemical synthesis of urea (Table S2, ESI†). Fig. S9 (ESI†) illustrates the FE occupancy of the CuRu-CBC sample at different potentials, indicating that the main competing reactions for the C–N coupling reaction are the HER and NO$_3$RR, with CO$_2$RR having a lower overall efficiency. The by-products at different potentials were CO, NO$_2^-$, NH$_4^+$ and H$_2$. Notably, NO$_3$RR was inhibited at −0.55 V (*vs.* RHE), suggesting the maximum C–N
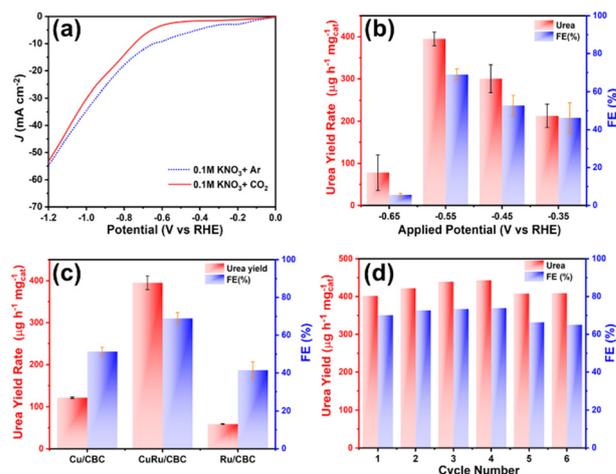

Fig. 3 (a) LSV curves of CuRu-CBC in 0.1 M KNO$_3$ electrolyte with Ar or CO$_2$ feeding gas. (b) Urea yield rate and FE of CuRu-CBC at different potentials. (c) Urea yield rate and FE at −0.55 V (*vs.* RHE) for Cu-CBC, CuRu-CBC and Ru-CBC samples. (d) Recycling stability test of CuRu-CBC.

coupling activity. Furthermore, Fig. 3c reveals that the electrocatalytic urea yield rate of CuRu-CBC is 3.26 and 6.71 times higher than Cu-CBC (120.94 ± 1.60 µg h^{-1} mg$_{cat}^{-1}$) and Ru-CBC (58.84 ± 0.92 µg h^{-1} mg$_{cat}^{-1}$), respectively. Importantly, the faraday efficiency of electrocatalytic urea for the CuRu-CBC sample is significantly higher than that of Cu-CBC (51.31 ± 2.28%) and Ru-CBC (41.49 ± 4.34%). In addition, the CuRu-CBC catalyst displays a very superior electrocatalytic activity for urea synthesis compared with that of Cu-CBC (120.94 ± 1.60 µg h^{-1} mg$_{cat}^{-1}$) and Ru-CBC (58.84 ± 0.92 µg h^{-1} mg$_{cat}^{-1}$), which can be attributed to the charge transfer between Cu and Ru inhibiting the competitive reactions and enhancing the C–N selectivity. Besides superior activity, the durability of the catalyst is another crucial parameter for a practical application. As shown in Fig. 3d, the CuRu-CBC sample maintains stable electrocatalytic C–N coupling activity after 6 cycling tests. Additionally, the yield of urea is linear with respect to reaction time (Fig. S10, ESI†), and chronoamperometric curves (Fig. S11, ESI†) demonstrate that the current density of the CuRu-CBC remains essentially unchanged during the 10 h test period. Furthermore, there is no change in the content of Cu and Ru in the CuRu-CBC before and after the reaction (Table S3, ESI†). After electrolysis, the high-resolution Cu 2p and Ru 3p XPS spectra were carried out to analyze the electronic properties of CuRu-CBC before and after the electrocatalytic process (Fig. S11b, ESI†). Interestingly, after electrocatalytic reaction, the Cu 2p significantly shifted towards lower binding energies, while the characteristic peaks of Ru 3p shifted to a higher binding energy (Fig. S11c, ESI†), indicating the existence of charge transfer from Ru atoms to Cu atoms during the electrocatalytic C–N coupling process. This will result in the Ru atom surface showing an electron-deficient state, which will further inhibit the occurrence of the HER and NO$_3$RR. In contrast, the surface of the Cu atoms will exhibit an electron-rich state, which facilitates the CO$_2$RR generation of *CO from CO$_2$ adsorbed on the surface of the Cu atoms. In addition to this, the electron transfer between Cu and Ru facilitates the optimisation of the reactive adsorption energy of the intermediates.[29]
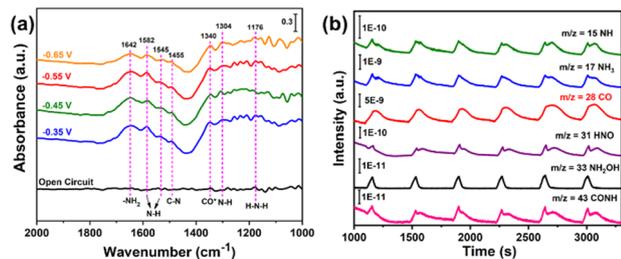
Fig. 4 (a) *In situ* ATR-SEIRAS spectra of CuRu-CBC from OCP to −0.65 V (*vs.* RHE) in electrolytes containing 0.1 M KNO_3; (b) *in situ* DEMS measurements over CuRu-CBC using CO_2 as the feed gas.

Thus, the electron transfer present within the CuRu-CBC is favourable for electrochemical urea synthesis.

To gain a deeper understanding of the electrocatalytic C–N coupling reaction mechanism of CuRu-CBC, CO_2-temperature-raising programmed desorption (CO_2-TPD) experiments were conducted. As depicted in Fig. S13 (ESI†), Cu-CBC, CuRu-CBC and Ru-CBC exhibit strong CO_2 adsorption peaks near 266 °C, attributed to CO_2 adsorption on CBC.[30] In the Ru-CBC samples, no other CO_2 adsorption peaks were observed, while Cu-CBC displayed CO_2 chemisorption peaks near 390 °C and 497 °C. This suggests that CO_2 has a higher affinity for Cu atoms, making it more easily adsorbed on the surface of Cu atoms. *In situ* ATR-SEIRAS measurements (Fig. S14, ESI†) of CuRu-CBC were employed to capture and monitor adsorbed C–N coupling reaction intermediates. As illustrated in Fig. 4a, for a given potential, the peak at 1340 cm^{-1} corresponds to the stretching vibration of CO*, while the peaks at 1582 cm^{-1}, 1545 cm^{-1} and 1304 cm^{-1} are attributed to the bending and stretching vibrations of N–H.[11,12,31] Additionally, the C–N stretching vibrational peak of free urea, located at 1455 cm^{-1}, as well as the stretching and bending vibrational peaks belonging to –NH_2, observed at 1176 cm^{-1} and 1642 cm^{-1}, provide direct evidence of urea production.[32] In Fig. S15 (ESI†), the signals of the C–N stretching vibrational peak at 1455 cm^{-1} and the stretching and bending vibrational peaks belonging to N–H at 1545 cm^{-1} and 1582 cm^{-1} gradually strengthen with the reaction time, further confirming that *CO and *NH are important intermediates in the synthesis of urea. *In situ* DEMS tests were performed to capture the intermediates (Fig. S16, ESI†) and molecular products during the electrocatalytic reaction (Fig. 4b). When CO_2 is introduced into the cell and the applied potential is switched, periodic detection of the signals at *m/z* 43, 33, 31, 28, 17 and 15 occurs. These signals can be assigned to *CONH, *NH_2OH, *NHO (equivalent to *HNO),*CO, *NH_2 and *NH intermediates.[33] The *in situ* DEMS and *in situ* ATR-SEIRAS results reveal the urea formation process, where CO_2 and NO_3^- undergo hydrogenation on the surface of CuRu-CBC, producing *CO and *NH intermediates, respectively. Subsequent C–N coupling leads to the formation of the *CONH intermediate. Significantly, the presence of the *CONH intermediate prevents excessive hydrogenation of *CO and *NH, thus avoiding the formation of by-products such as CO and NH_3, and ultimately resulting in urea production.

In conclusion, the CuRu nanoalloy loaded on carbonized bacterial cellulose exhibited both high reactivity and stability in the electrocatalytic C–N coupling reaction. The unique inner-boundary electric field structure of CuRu-CBC facilitated the easier reduction of CO_2 molecules adsorbed on the surface of Cu atoms. Moreover, the electron transfer between the Cu and Ru interface could inhibit the competitive reaction, resulting in high selectivity and FE of CuRu-CBC for urea synthesis. This work not only demonstrates the potential of CuRu-CBC as an electrocatalyst but also opens up new avenues for the design of electrocatalytic C–N coupling materials in the future.

Jiafang Liu: conceptualization, investigation, visualization, writing – original draft. Shengbo Zhang: data curation, resources, supervision, writing – review & editing. Yong Jiang: investigation, resources, formal analysis. Wenyi Li: investigation. Meng Jin: visualization. Jun Ding: investigation. Yunxia Zhang: software. Guozhong Wang: software. Haimin Zhang: funding acquisition, supervision, resources, writing – review & editing.

Data availability

The data supporting this article have been included as part of the ESI.†

Conflicts of interest

There are no conflicts to declare.

Notes and references

1 X. Zhang, *et al.*, *Nature*, 2015, **528**, 51–59.
2 S. Zhou, *et al.*, *J. Am. Chem. Soc.*, 2020, **142**, 308–317.
3 C. He, *et al.*, *ACS Catal.*, 2019, **9**, 7311–7317.
4 B. H. Ko, *et al.*, *J. Am. Chem. Soc.*, 2022, **144**, 1258–1266.
5 S. Yang, *et al.*, *Angew. Chem., Int. Ed.*, 2023, **62**, e202312076.
6 C. Lv, *et al.*, *ACS Nano*, 2022, **16**, 8213–8222.
7 S. Shin, *et al.*, *Energy Environ. Sci.*, 2023, **16**, 2003–2013.
8 Y. Feng, *et al.*, *Nano Lett.*, 2020, **20**, 8282–8289.
9 X. Chen, *et al.*, *Proc. Natl. Acad. Sci. U. S. A.*, 2023, **120**, e2306841120.
10 X. Wei, *et al.*, *J. Am. Chem. Soc.*, 2022, **144**, 11530–11535.
11 C. Chen, *et al.*, *Nat. Chem.*, 2020, **12**, 717–724.
12 L. Pan, *et al.*, *Angew. Chem., Int. Ed.*, 2023, **62**, e202216835.
13 P. Xing, *et al.*, *ACS Appl. Mater. Interfaces*, 2023, **15**, 22101–22111.
14 S. Fu, *et al.*, *Chem. Commun.*, 2023, **59**, 4344–4347.
15 Y. Gao, *et al.*, *Nano-Micro Lett.*, 2023, **15**, 158.
16 Y. Li, *et al.*, *Nat. Commun.*, 2024, **15**, 176.
17 H. Wang, *et al.*, *Appl. Catal., B*, 2022, **318**, 121819.
18 F. Song, *et al.*, *ACS Mater. Lett.*, 2022, **4**, 967–977.
19 Z. Zhang, *et al.*, *Int. J. Hydrogen Energy*, 2024, **74**, 10–16.
20 S. Tang, *et al.*, *J. Colloid Interface Sci.*, 2024, **669**, 228–235.
21 X. Zhang, *et al.*, *Nat. Commun.*, 2022, **13**, 5337.
22 J. Zheng, *et al.*, *Appl. Catal., B*, 2023, **338**, 123056.
23 W. Yu, *et al.*, *Energy Environ. Sci.*, 2023, **16**, 2991–3001.
24 J. Fang, *et al.*, *Nat. Commun.*, 2022, **13**, 7899.
25 S. Zhang, *et al.*, *Angew. Chem., Int. Ed.*, 2020, **59**, 13423–13429.
26 C. Zhang, *et al.*, *Colloids Surf., A*, 2023, **666**, 131311.
27 T. Wu, *et al.*, *J. Hazard. Mater.*, 2022, **438**, 129551.
28 Q. Gao, *et al.*, *Nat. Commun.*, 2022, **13**, 2338.
29 L. Tao, *et al.*, *Adv. Energy Mater.*, 2019, **10**, 1901227.
30 S. Zhang, *et al.*, *EES Catal.*, 2023, **1**, 45–53.
31 C. Lv, *et al.*, *Nat. Sustainability*, 2021, **4**, 868–876.
32 N. Li, *et al.*, *Sci. China: Chem.*, 2023, **66**, 1417–1424.
33 Y. Huang, *et al.*, *ACS Energy Lett.*, 2021, **7**, 284–291.